Article:
Kłosowski, MM, McGilvery, CM, Li, Y et al. (2016) Micro-to nano-scale characterisation of polyamide structures of the SW30HR RO membrane using advanced electron microscopy and stain tracers. Journal of Membrane Science, 520. pp. 465-476. ISSN: 0376-7388

https://doi.org/10.1016/j.memsci.2016.07.063

Micro- to nano-scale characterisation of polyamide structures of the SW30HR RO membrane using advanced electron microscopy and stain tracers

Michał M. Kłosowski[1], Catriona M. McGilvery[1], Yuqiong Li[2], Patricia Abellan[3], Quentin Ramasse[3], João T. Cabral[2], Andrew G. Livingston[2], and Alexandra E. Porter[1]*

[1] Department of Materials and Engineering, Imperial College London, London

[2] Department of Chemical Engineering, Imperial College London, London

[3] SuperSTEM Laboratory, Daresbury

*Corresponding author: Alexandra E. Porter, Department of Materials and Engineering, Imperial College London, Royal School of Mines, South Kensington Campus, London, SW7 2AZ, UK; phone: (+44)207594 9691; e-mail: a.porter@imperial.ac.uk

Abstract

The development of new reverse osmosis (RO) membranes with enhanced performance would benefit from a detailed knowledge of the membrane structures which participate in the filtration process. Here, we examined the hierarchical structures of the polyamide (PA) active layer of the SW30HR RO membrane. Scanning electron microscopy combined with focused ion beam milling (FIB-SEM) was used to obtain the 3-D reconstructions of membrane morphology with 5 nm cross-sectional resolution (comparable with the resolution of low magnification TEM imaging in 2D) and 30 nm slice thickness. The complex folding of the PA layer was examined in 3 dimensions, enabling the quantification of key structural properties of the PA layer, including the local thickness, volume, surface area and their derivatives. The PA layer was found to exhibit a much higher and convoluted surface area than that estimated *via* atomic force microscopy (AFM). Cross-sectional scanning transmission electron microscopy (STEM) was used to observe the distribution of a tracer stain under various conditions. The behaviour of stain in dry and wet PA indicated that the permeation pathways have a dynamic nature and are activated by water. High resolution STEM imaging of the stained PA nano-films revealed the presence of <1nm pore-like structures with a size compatible with free volume estimations by positron annihilation lifetime spectroscopy (PALS). This study presents a comprehensive map of the active PA layer across different length scales (from micro- to sub-nanometer) and mechanistic insight into their role in the permeation process.

Keywords:

RO membrane, characterisation, FIB-SEM, STEM, permeation

1. Introduction

Reverse osmosis (RO) membrane filtration is frequently utilised in water purification and recycling for domestic, industrial and agricultural purposes [1,2]. Membranes designed for molecular separations in water usually comprise a “tight” separating layer of polyamide (PA) on a more open support layer of polysulfone (PSf). The PA and PSf layers are mounted on a woven fabric backing of polyethylene (PE) or polypropylene (PP) [3,4]. The topmost PA layer is thought to play the active role in the filtration process as a molecular sieve and an ion barrier [5]. Improved knowledge of the structure and chemistry of the PA layer is required to design membranes, which achieve higher performance in water desalination and purification [6]. Characterisation of the PA layer is particularly challenging due to its complex and interconnected ridge-valley structure, thinness of the active film, the sub-nanometre size of structures within the film, and beam sensitivity intrinsic to polymer materials in electron and ion beam microscopes.

The organisation of the PA layer at the meso-scale is often assessed by cross-sectional transmission electron microscopy (TEM) [7,8], isometric or top-down scanning electron microscopy (SEM) imaging [3,9–11] supported by topological information acquired *via* atomic force microscopy (AFM) [5,9,11,12]. The overall thickness of the PA layer ranges from 20 to 400 nm [12]. PA morphology is typically estimated by the maximum ridge-to-valley distance, average roughness and apparent surface area [5,13]. It is commonly accepted that water permeability increases with the apparent surface area of the PA layer [1].

The inner structures of the PA layer are usually characterised using electron microscopy (EM) imaging of membrane cross-sections [5]. The PA layer might be divided in two regions: a relatively flat and semi-porous base at the PA-PSf interface and a more open structure of

protuberances spreading from the base, giving rise to the well-known ridge-valley structure [14]. Recently, it has been suggested that the PA layer is formed of a continuous sub-10 nm, highly crumpled PA nano-film [15]. The crumpling of the thin nano-film results in the formation of multiple voids within the PA layer, especially in the basal region. Some studies suggest that these voids contribute to an increase in surface area (as the voids are open to the surface at one end [6,16]), which might be connected with increased flux [17–19]; other studies suggested that the voids are discrete [19,20].

The molecular-scale mechanisms of particle/ion filtration are not fully understood and are typically rationalised in terms of classic pore-flow or solution-diffusion models [21,22]. Separation studies postulated that permeation is modulated by both continuous pores and the density of cross-linked polyamide [23,24]. Molecular dynamics (MD) simulations suggested that the filtration occurs through a network of sub-nanometre pores, which may play an active or passive role in the process [25,26].

"Porosity" at such small length scales likely corresponds to a modulation of density and free volume inherent to polymeric networks, rather than to actual pores in the macroscopic sense. In addition, segmental and cooperative polymer dynamics, under solvation and pressure conditions, might be expected to modulate solute transport [27]. Evidence of sub-nanometre pores within the PA layer has been obtained by positron annihilation lifetime spectroscopy (PALS) [5,22,28] and solution permeation rate calculations [29]. Until now, the only spatially resolved imaging methods used to study pores smaller than 10 nm were based on the tracking of nanoparticles [30].

Few attempts have been made to validate the permeation models (pore flow *vs.* solution diffusion) described above. Nanoparticles have been used as contrast agents in attempts to map classic pores and/or permeation pathways within the PA and PSf layers. To enhance the

visibility of these structures in transmission electron microscopy (TEM), membranes were infiltrated with nanoparticles such as Au or OsO_2 [14,30]. These studies used particles of known size to visualise the crumpled topography of the PA layer [14] and to measure the sizes of pores in the PA layer [30]. As the nanoparticles are often inhomogenously distributed within the membranes, it is difficult to observe the direct transport pathways or draw conclusions about the behaviour of membranes during the filtration process. Furthermore, nanoparticles of set size may not accurately reflect the size of voids within the membrane, due to complex transport mechanisms, the variation in the sizes of the pores or the dynamic nature of these pores.

In addition to nanoparticles, heavy metal stains such as osmium tetroxide, ruthenium tetroxide, uranyl acetate or lead citrate may be used to reveal the structural features of the PA layer. By contrast to nanoparticles, metal stains diffuse more homogeneously through the material due to their small size (initially ionic); selectively lodge in charged regions; additionally fix the material and could be delivered in both liquid and vapour phases. To date, staining has mainly been used to enhance contrast of membranes in TEM and map the distribution of functional groups in the PA layer [7,12,14]. As most of the TEM studies were conducted at relatively low magnifications, it is difficult to characterise any structural features smaller than 30 nm.

The question of how the micro- to nano-metre scale features and their morphology modulate the permeation process remain unanswered [6]. Spatially resolved imaging techniques, such as SEM, TEM or AFM, do not provide a complete picture of the 3-dimensional (3-D) architecture of the PA layer and the impact of the structures within the PA on the filtration process at the micro- to nano-scale. At the sub-nanometre scale, little is known about the 3-D distribution of the pores, their chemistry and role in solute (water/ion) transport. PALS studies provide only statistical information about the bulk of the

membrane and computational models generally lack validation with spatially resolved experiments.

High resolution electron microscopy (EM) studies of RO membranes are so far limited. EM has mainly been used for relatively low magnification, bright-field TEM imaging showing cross-sections of commercial membranes [5,14] or SEM imaging of the PA surface [10,11]. However, EM methods are exceptionally well-suited to provide spatially resolved maps of the hierarchical structures of the polyamide layer. Advanced nanoanalytical techniques, available on modern scanning TEMs (STEMs), have a spatial resolution sufficient to observe structural features smaller than 1 nm.

The combination of tomographic EM methods allows 3-D visualisation of hierarchical membrane features from the micro- to nano-metre length scales. Yan *et al.* [16] highlighted the significance of large voids (10-50 nm in diameter) within the PA layer and the possible pathway in the BW30 membrane. Pacheco *et al.* [19] have recently examined void spaces (15 to 30 nm in diameter) within the PA layer of ESPA3 and SWC3 in 3-D and proposed a link between an increased volume of these voids with increased permeance of the membrane. A 2-D study by Lin *et al.* [20] estimated that these voids may constitute up to 30% of the PA layer volume. The focus of our work is therefore to comprehensively examine and precisely quantify the structures within the PA layer envelope at the micro-scale, and examine structures within the PA nano-film at the nano- to sub-nano-scale with unprecedented spatial resolution.

We combine a range of EM techniques with heavy metal staining methods to visualise the hierarchical structure of the PA layer of the commercially available SW30HR (Dow Filmtec) membrane, selected for its common industrial use in high rejection water desalination [31].

Focused ion beam scanning electron microscopy (FIB-SEM) was used to reconstruct the features of polyamide in 3-D with high spatial resolution. Staining was used not only for contrast enhancement, but also for elucidation of the PA structure, specifically for mapping the nano-pores within the PA nano-film using high annular dark field scanning transmission electron microscopy (HAADF-STEM; atomic number, Z^2 contrast imaging). Moreover, by varying the staining methods, potential permeation mechanisms in the polyamide film could be proposed.

2. Materials and methods

2.1. Sample preparation for electron microscopy

SW30HR (Dow Chemical Company, USA) flat sheet membranes were stained with RuO_4. In general, staining improves the overall contrast for electron microscopy (EM) imaging, stabilises the polymer under the electron beam (by crosslinking oxidised moieties, such as amide and carbonyl groups) and highlights the distribution of functional groups. The varying behaviour of stain tracers in different staining conditions may also reveal the permeation pathways.

1x1 cm^2 membrane coupons cut from a larger sheet were stained using standard (as received) stabilized 0.5 wt.% aqueous solutions of RuO_4 (Acros Organics, Geel, Belgium). Four different staining methods were used:

I. A membrane coupon was fully immersed in liquid stain for 5 min and immersed in 10ml of water for 30 min;
II. The top surface of membrane coupon was exposed to the stain vapours for 1 min;
III. A drop of liquid stain was placed on the top surface of membrane coupon for 1 min;

IV. A drop of pure water was placed on the top of the membrane coupon for 10 min, and then the top surface of the coupon was exposed to the stain vapours for 1 min.

Method I was used to enhance contrast for FIB-SEM imaging (SI Figure 1) to ensure that the polymer was stained throughout. Methods II, III and IV were used to examine permeation pathways within the PA layer by STEM. To ensure the reproducibility of the results, 3 samples for each of the staining conditions were prepared. The combination of dry (method II) and wet techniques was used to probe the transport mechanisms of ions and to highlight the role of water in the permeation process. Staining was performed under ambient conditions. Longer staining times (5 and 10 min) were also tested for methods II-IV.

To prepare samples for EM, the stained samples were washed 3 times with water for 5 min each to remove excess stain. Next, to dehydrate the samples, they were immersed in 50%, 70%, 90% and 100% aqueous solutions of ethanol (30 min each). Samples were embedded in LR White Hard resin (London Resin Company, Reading, UK), which was found to give the best contrast from the PA polymer. Samples were immersed successively in 1:1 and 3:1 resin:ethanol solutions for 12h. For the next 4 days, samples were immersed in pure resin to ensure full infiltration. The resin was changed every 24h. On the last day samples in resin were degased under vacuum to ensure sample-resin binding and resin hardening. The final resin batch was mixed with a dedicated LR White accelerator (benzoyl peroxide) to enhance the crosslinking of the resin at room temperature. Pristine (non-stained) samples were embedded using the same protocol.

2.2. Focused ion beam SEM (FIB-SEM)

For FIB-SEM milling, a flat surface of the resin embedded sample stained, using method I, was exposed using a PowerTome ultramicrotome (Boeckeler Instruments, Tucson, USA) with a

diamond knife (DiATOME, Hatfield, USA). Next, a 1 mm thick slice was cut and mounted on an aluminium stub using silver paint. Prior to SEM imaging, the sample was coated with a 20 nm layer of chromium to reduce charging.

FIB-SEM series were taken on an Auriga microscope (Carl Zeiss Microscopy, Jena, Germany) fitted with a gallium ion source. The FIB milling conditions were set to 30 kV and with a beam current of 1 nA, which results in a probe size of ~10nm.

Samples were milled from the side (SI Figure 2). To minimise FIB damage (*e.g.*, ion implantation and curtaining) during alignments, the top, 1µm-thick part of sample was used as a sacrificial layer. Only the region below the sacrificial layer was imaged by SEM (SI Figure 2).

SEM imaging was performed at 1.49 kV with an energy selective backscattered electron detector. In these conditions, the size of SEM probe is ~2nm. Pixel averaging collection was used to reduce noise. In total, 357 images of membrane cross-sections were acquired, with a step size of 30 nm between successive images. As SEM images were taken at an angle (SI Figure 2), the images had to be adjusted to account for this resulting in non-uniform pixels (the pixel size in y direction was multiplied by1.24).

Avizo software (FEI, Hillsboro, USA) was used for pre-processing of FIB-SEM data and reconstruction of virtual volumes. FIB-SEM slices were denoised using a Gaussian filter and realigned using an automatic least-squares function. Further information on thresholding and reconstruction can be found in SI (SI Figure 3). The reconstructed voxel size was 3.7x4.6x30 nm^3.

2.3. Estimation of structural properties

To minimise errors in the calculation of membrane parameters arising from non-uniform voxels [32], volumes reconstructed from FIB-SEM data were resliced in ImageJ [33] to obtain uniform voxels of 5x5x5

nm^3. To accurately assess the outer volume of the PA layer envelope and the impact of the discrete objects within the envelope on the structural parameters, the volume was purified (discrete voids and particles were removed from the volume – SI Figure 4) in BoneJ [34]. The PA layer is very heterogeneous; to address the natural variability of the membrane, 2.5x2.5 μm^2 regions were examined.

BoneJ was used to determine the total surface area (SA), volume (V) and local thickness [35] distribution of the PA layer envelope. The local thickness at any given point (voxel) of a 3-D structure is defined as the diameter of the largest sphere that fits inside the 3-D object and contains the point [35]. In other words, the individual local thickness measurement represents the local diameter of the structure. A graphic explanation of the local thickness measurement is given in SI Figure 5. The rudimentary reactivity was estimated as surface-to-volume (SA/V) ratio. Front and rear surface areas were calculated from the total surface area of front and rear volumes by subtracting the side and division areas (SI Figure 4). Relative area ratios were calculated by dividing the actual surface area by the area of the underlying rectangle.

2.4. Atomic force microscopy (AFM)

For comparison with the surface structure generated from FIB-SEM, AFM imaging was used. The front surface of the PA layer was imaged on the original SW30HR membrane taped to an AFM sample holder with the PA facing upwards. To image the rear surface of the PA layer, free-standing PA layers were prepared and placed on a glass cover slip. The freestanding membranes were obtained as follows.

The polyethylene (PE) backing was carefully peeled off of the SW30HR membrane with a scalpel blade. The remaining two-layered membrane was pressed onto a clean glass cover slip such that the PA side sticks to the glass substrate. A drop of deionized water was added to hydrate and soften the membrane. A few drops of

dimethylformamide (DMF) were carefully placed onto the PSf facing upwards. As the PSf dissolved in the solvent, the glass slide was tilted to allow the solvent with the dissolved PSf to be drained. The process was repeated several times until the PSf was completely removed. The isolated PA thin layer appeared optically transparent.

Samples were imaged in an Innova AFM (Bruker, USA) in tapping mode fitted with a phosphorus (n) doped silicon cantilever (k = 20-80 N/m, tip nominal diameter <10 nm). AFM images were acquired at 512 samples/line and a scanning rate of 0.2 Hz, under ambient conditions.

2.5. Scanning transmission electron microscopy (STEM)

For TEM imaging, thin (~70 nm) sections of samples were cut with the ultramicrotome (Boeckeler Instruments, Tucson, USA) and transferred onto 300-mesh copper grids with a lacey carbon film support (TAAB Laboratories Equipment, Aldermaston, UK).

STEM imaging was performed on a C_s (image-)corrected, FEI Titan 80-300 microscope operated at 80 and 300kV. A 60 mm camera length was used giving an annular dark field (ADF)-STEM collection semi-angle of 26-145 mrad and high angle (HA)ADF-STEM collection semi-angle of 129-575 mrad. Before imaging, samples were beam showered (exposed to an uncondensed broad electron beam) in the TEM mode to stabilise the sections by equalizing the charge distribution across the section and reduce hydrocarbon contamination [36]. The experimental dose was closely monitored and did not exceed 1250 e/nm^2.

High resolution STEM imaging was performed on SuperSTEM2 - Nion UltraSTEM 100 microscope at 100kV. The HAADF collection semi-angle range is 85-190 mrad and the probe size is 0.1 nm. Prior to imaging, samples were baked for 12h in a vacuum oven (10^{-6} Torr) with a rising temperature gradient (from room temperature to 130°C) to reduce hydrocarbon contamination.

2.6. Quantification of the <1 nm structures

High resolution images were denoised using a Gaussian filter, contrast-enhanced and thresholded using magic wand selection. We aimed to highlight only structures that showed local maxima. In some instances we used a water-shedding algorithm to separate larger clusters of stain precipitates. The surface areas of the reconstructed precipitates were calculated using ImageJ (SI Figure 6). The diameters of the pores were estimated as the diameter of circles of the same area. All spots of diameter smaller than 0.2 nm were filtered out (the approximate size of Ru atoms ≈ 0.15 nm).

3. Results

3.1. 3-D structure of the polyamide layer

To reconstruct and quantify features of the PA layer morphology, cross-beam FIB-SEM tomography was used. We are able to visualise features larger than 15 nm in the PA layer in 3-D. The 3-D reconstruction in Figure 1 and SI Movie 1 shows the front (Figure 1A) and rear (Figure 1B) surface, and cross-sections (Figure 1 C, D) of the PA envelope. The envelope represents a volume containing the entire PA layer with the discrete, inner voids excluded. Orthoslices taken through the 3-D reconstructions show that protuberances, which are often referred to as ridges [5], are in fact leaf-like (bridge-like) sheets overhanging large regions of the PA layer (Figure 1 C, D - arrowheads). These regions are not fully enclosed and large empty spaces directly underneath the ridges are open to the front surface. There were also smaller, discrete voids observed within the PA envelope (Figure 2 and SI Movie 2). These discrete voids have an average local thickness of 21±7 nm (367 voids for the minimal threshold) and 17±5 nm (61 voids for the maximal threshold).

Local thickness mapping [34] was also performed on the bulk features of the PA layer (Figure 3A, B and C). The local thickness describes dimensions of all PA layer features: from a single sheet (~10 nm) to

multiple convoluted and compacted sheets of PA nano-film (~260 nm). The latter structures appear as non-porous (Figure 3 B, E – white arrowheads), but may possess void spaces, which are below the resolution of the FIB-SEM technique or remain unresolved due to poor contrast.

The ridge-like features (Figure 1A and C) on the front side of the membrane were found to be <70 nm thick, whereas the features on the rear side of the PA layer were much thicker (up to 260 nm), as AFM cannot measure overhangs, steep walls and other convoluted structures of the PA topography. For comparison, AFM maps were converted into 3-D models and local thickness maps were calculated (Figure 3D, E and F). The measured root-mean square roughness was 75 nm and the peak-to-peak height was 496 nm for the front surface, and 15nm and 110nm, respectively, for the back surface. In the AFM reconstruction, almost all of the membrane volume appeared thick (bright), because this method only maps the apparent topography. In Table 1, the structural properties of the PA layer in the SW30HR membrane are given.

Table 1 Structural properties of the PA layer of a SW30HR membrane (for 2.5x2.5 µm^2 regions).

	Mean local thickness (nm)	Maximal local thickness (nm)	Reactivity SA/V (nm^{-1})	Relative area ratio - front	Relative area ratio - rear
PA envelope (MIN*)	96±42	206	0.037	6.71	1.87
PA envelope (MIN Purified)	125±61	260	0.033	5.98	1.67
PA envelope	179±92	344	0.028	4.9	3.55

(MAX)					
PA envelope (MAX Purified)	183±90	344	0.025	4.66	2.64
AFM	284±71	443	0.012	1.71	1.3**
AFM Purified	285±70	443	0.012	1.64	1.3**

* MIN – minimal threshold, MAX – maximal threshold, Purified – discrete voids removed

** AFM front and rear surface images were collected from different regions.

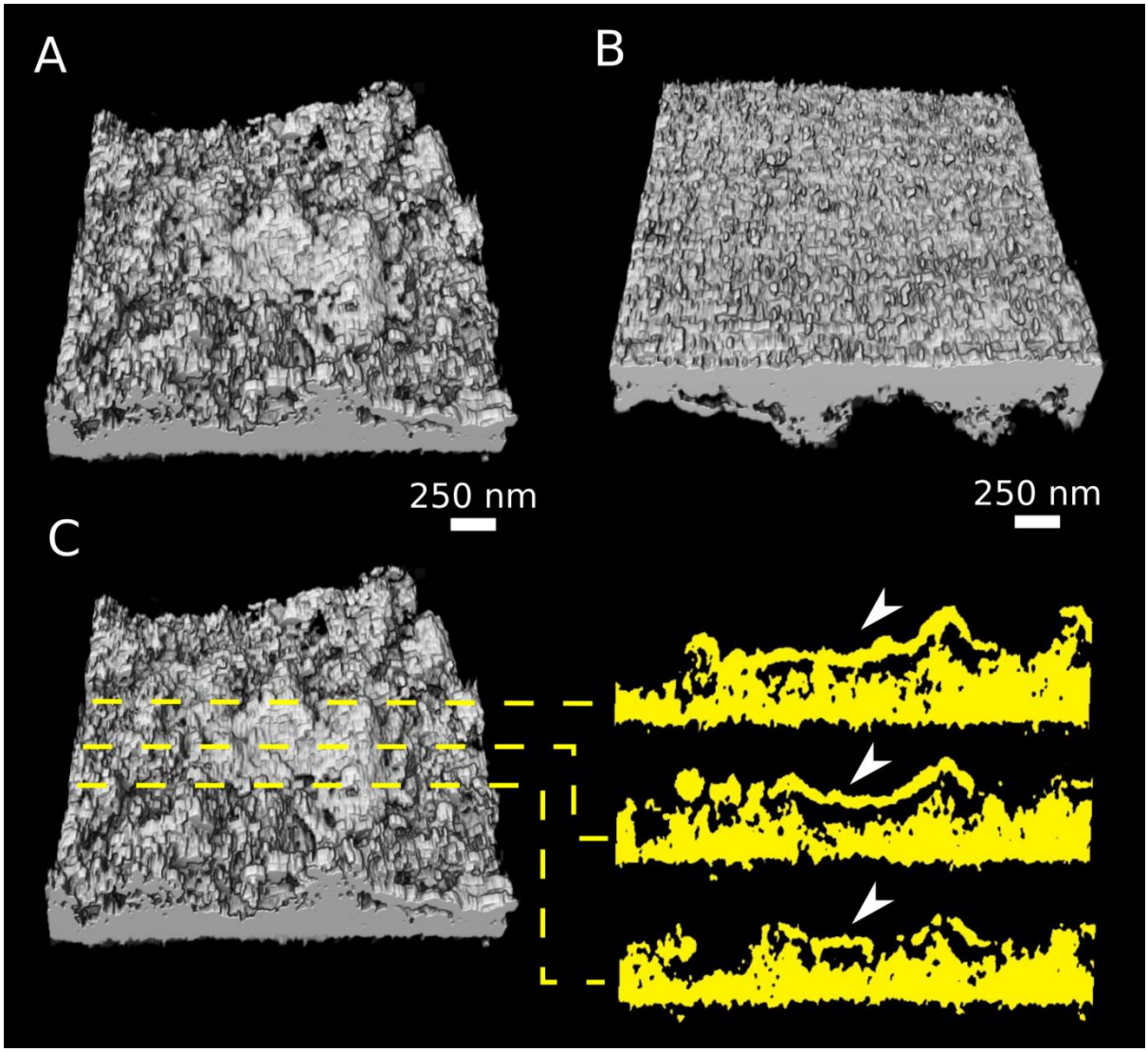

Figure 1 A FIB-SEM 3-D reconstruction of the PA layer envelope showing: (A) the front and (B) rear surfaces of the PA and (C) cross-sections through the ridges showing that they are hollow (white arrowheads). All voids seen in (C) are open to the surface.

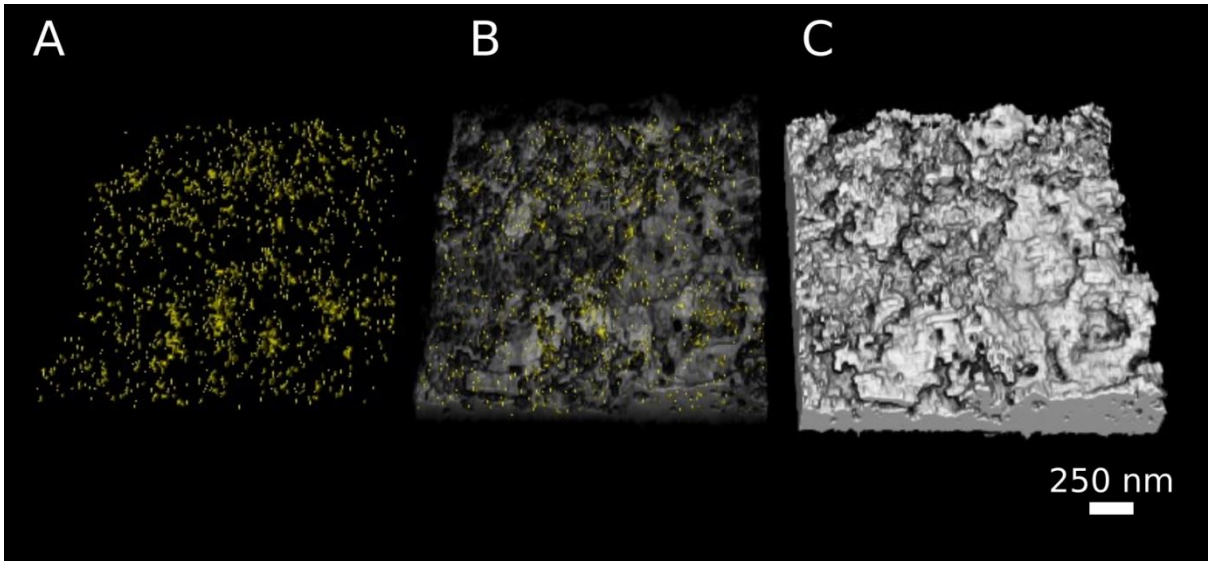

Figure 2 A FIB-SEM 3-D reconstructions of discrete voids (yellow) and the PA envelope (grey). (A) Discrete voids extracted from the PA reconstruction through a purification routine. (B) The same voids (A) overlaid with a semi-transparent PA envelope. (C) A fully opaque reconstruction of the PA envelope in the given region.

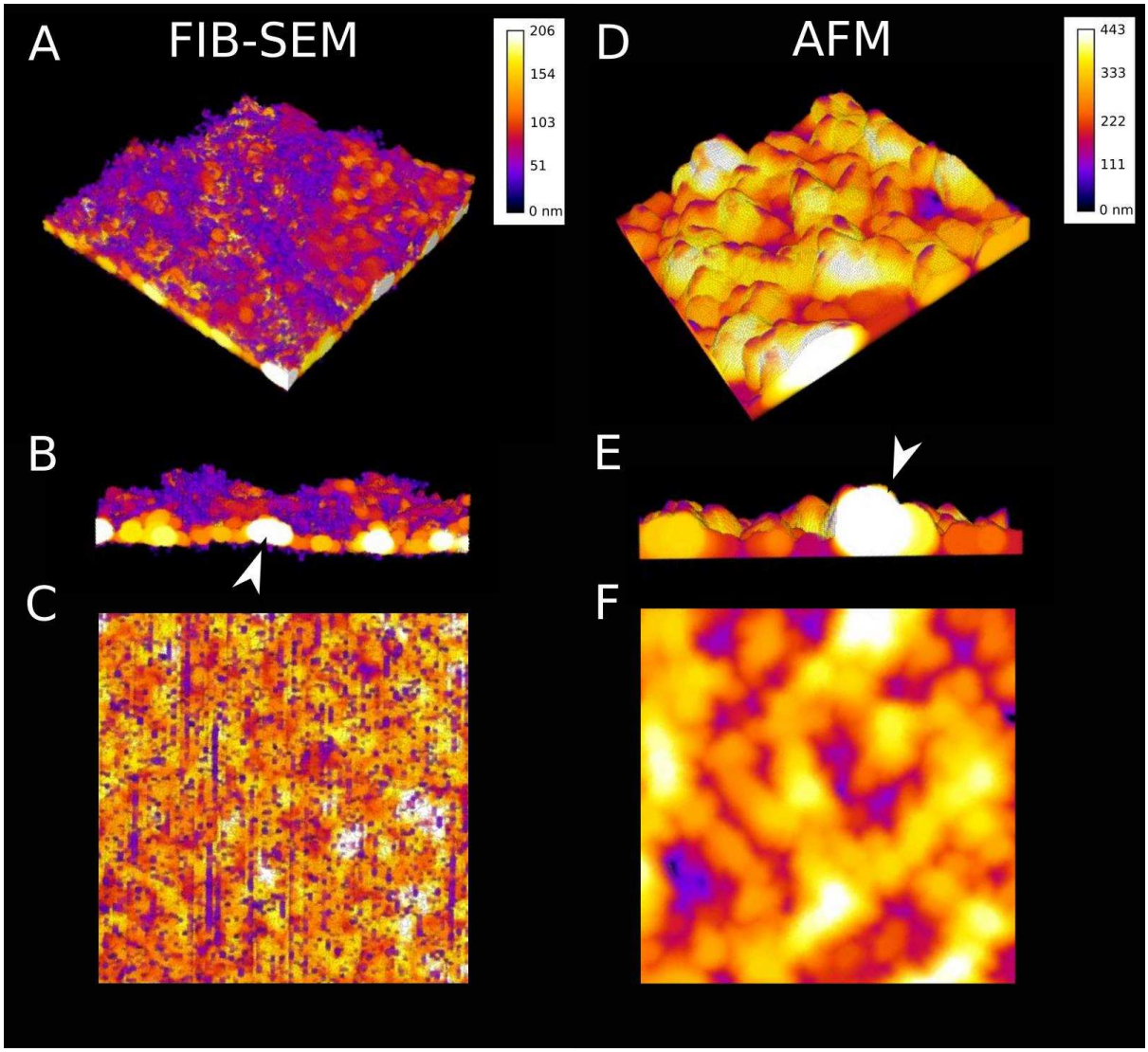

Figure 3 A local thickness map of the PA envelope: (A) an isometric, (B) side and (C) a rear view from a FIB-SEM reconstruction and (D) an isometric, (E) side and (F) a rear view from an AFM reconstruction. Thin regions are dark (red to violet), while thick regions are bright (white to yellow; the thickest structures for each reconstruction are indicated by white arrows). Each view shows a 2.5x2.5 μm^2 region.

3.2. Inner structure of PA layer

Staining experiments were used to reveal the inner structures of the PA layer, seeking to resolve possible permeation pathways, and thus, transport mechanisms through the PA nano-film.

In Figure 4, the effects of vapour staining on a dry membrane (method II) are shown. As the vapour stain reached the top surface of the membrane, stain propagation was evidently hindered at the PA-air boundary. The stain did not penetrate readily into the PA nano-film and instead precipitated forming a bright crust along the top interface (Figure 4 A, B). Bright spots within the PA nano-film were also observed (Figure 4C), suggesting that some stain precipitated within the pores of the PA. Many of the voids observed at the rear side of the PA layer (*i.e.*, inside the basal region next to the polysulfone support) were not accessed by the stain. Stain precipitates were observed in only a few of these voids (Figure 4A, arrowheads), which are most likely open to the top surface. Occasionally, stain precipitates aggregated at the entrance to a seemingly open void (Figure 4D and SI Movie 3). In general, the propagation of stain through a dry PA layer was significantly impeded.

The liquid staining technique (method III) sought to visualise the transport of water in the PA layer. As the stain is in an aqueous solution, the distribution of tracer should, in principle, reflect the fraction accessible to water molecules within the PA layer. In Figure 5, the effects of liquid staining on the front side of the membrane are shown, in clear contrast to the dry images above. When the liquid stain was applied on the top surface, the stain propagated through the PA layer and into the PSf support. Voids on the rear side of the PA layer (towards the PA/PSf interface) and very complex structures within the PA were penetrated by the stain (Figure 5 A, C). Staining highlighted the presence of effective “channels” within the PA layer (Figure 5 B, D), which were either filled with a dense precipitate (black arrowheads) or were empty (white arrowheads). Such ”channels” were also observed in non-stained samples (Figure 6), but staining significantly enhanced their visibility. These structures have significantly weaker contrast in the pristine (non-stained) PA, which

suggests that these are hollow regions formed by tight folding of the PA film.

The staining patterns clearly differed between the dry and wet experiments presented above. Therefore, membrane solvation and swelling in water and must play a significant role in activating the permeation pathways within the PA. To test this hypothesis, the vapour staining technique on a wet membrane (method IV) was used to further investigate the role of water and access of transport pathways in the membrane. In Figure 7, the effects of vapour staining on a wetted membrane were shown. In comparison to the dry membrane (Figure 4) the stain started to reach enclosed regions of the PA layer (Figure 7A), but did not penetrate the PA as thoroughly as under wet conditions (Figure 5). Smaller precipitates within the PA nano-film were often observed and occasionally, a stain propagation front could be seen (Figure 7B).

For longer staining times (5 and 10 min), precipitates outside the PA layer dominated the contrast (SI Figure 7).

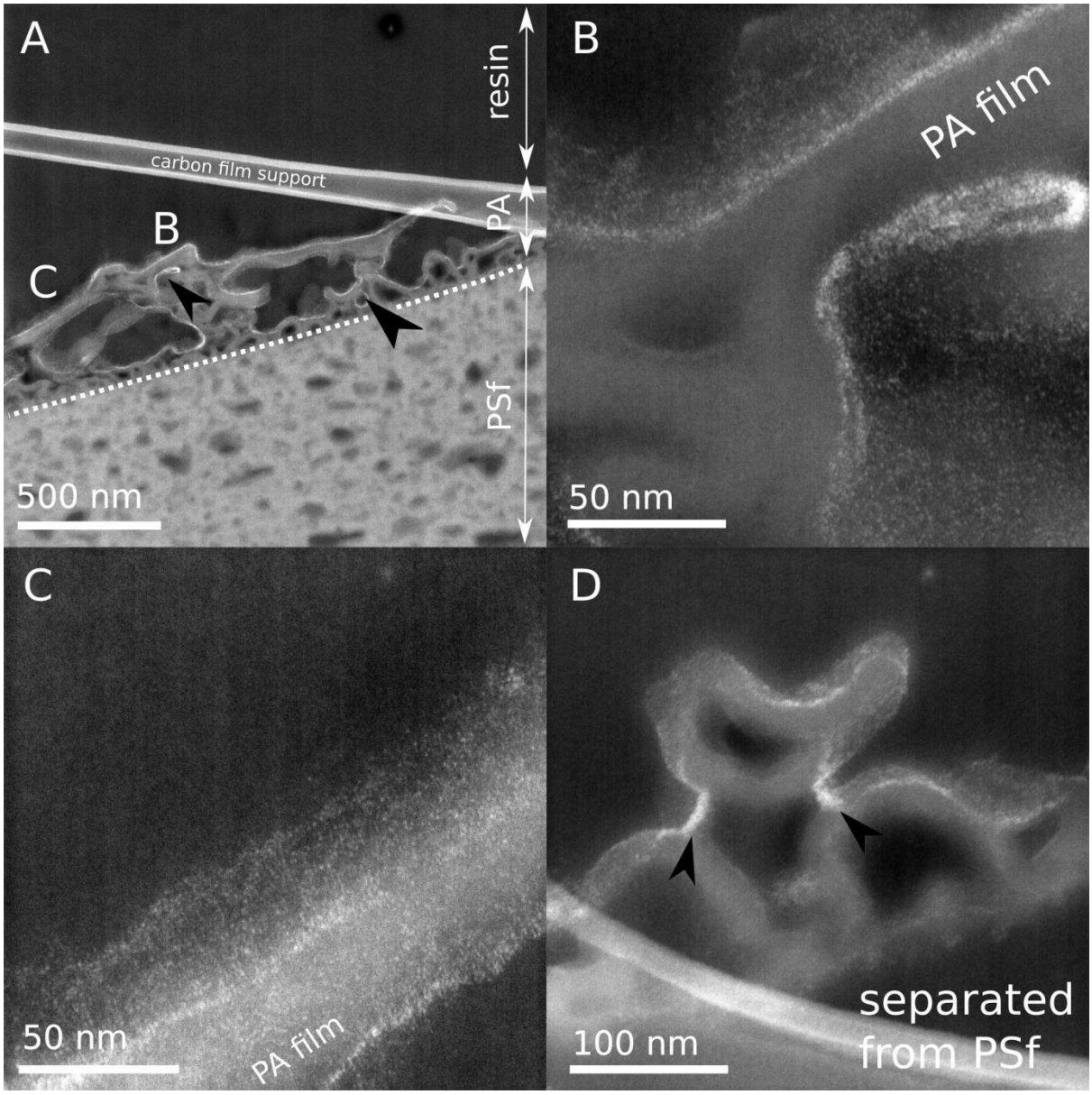

Figure 4 HAADF-STEM images of a dry SW30HR membrane, which was vapour stained on the front side with RuO_4 for 1 min. (A) Stain precipitates formed on the surface of the PA layer and within few voids (black arrowheads) within the layer. The dotted line represents the PA/PSf interface. (B) Higher magnification image of the region seen in (A) showing stain on the outside of the nano-film. (C) Higher magnification image of the region seen in (A) showing stain precipitates within the PA nano-film. (D) Stain precipitates aggreagating (black arrowheads) in the entrance to a seemingly open void.

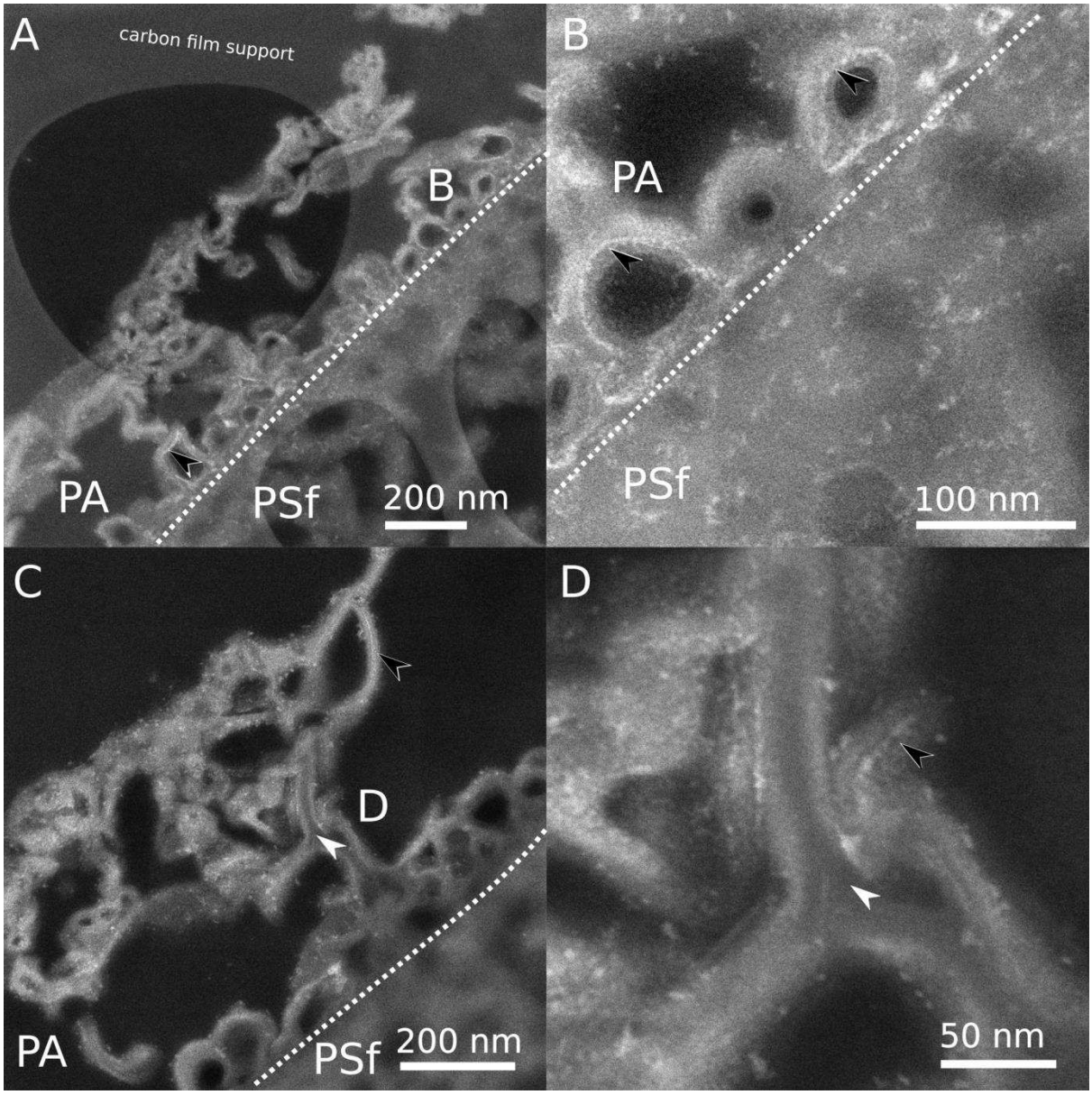

Figure 5 HAADF-STEM images of a SW30HR membrane stained from the front side with RuO_4 in aqueous solution for 1 min. (A) Stain precipitates were present in the whole volume of the PA layer. (B) Higher magnification image of the region seen in (A) showing dense precipitates (black arrowheads) formed within "channels" of the basal PA layer. (C) Selective staining showing empty (white arrowheads) and occupied (black arrowheads) "channels" within the PA. (D) Higher magnification image of empty (white arrowheads) and filled (black arrowheads) channels seen in (C). The dotted lines in (A), (B) and (C) represent the PA/PSf interface.

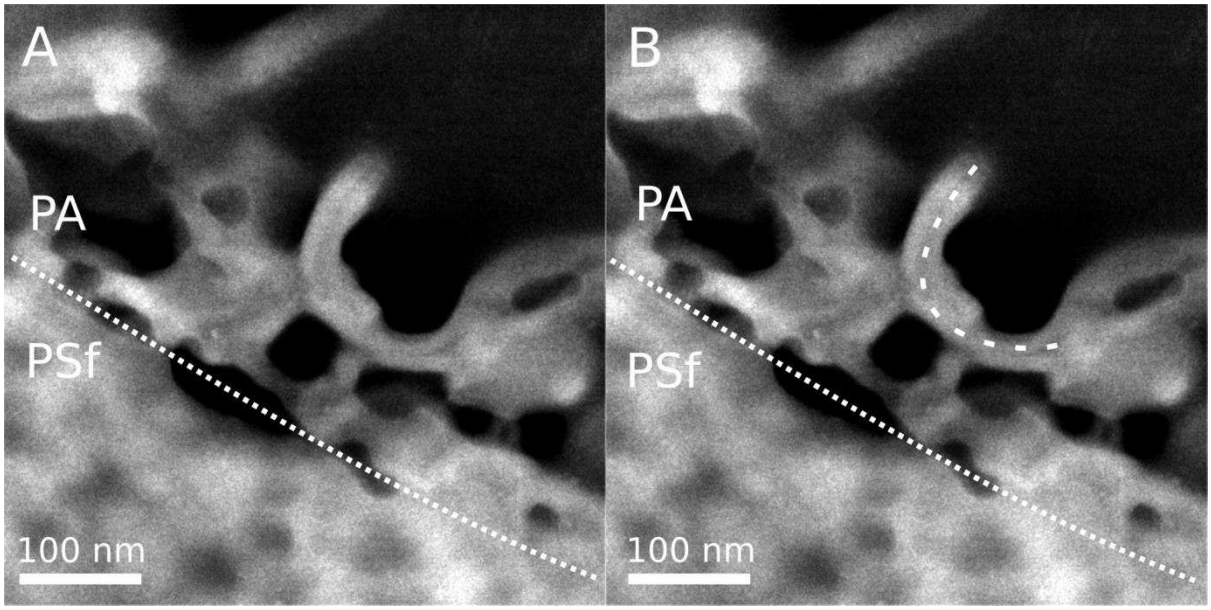

Figure 6 HAADF-STEM images of a non-stained SW30HR membrane. (A) An acquisition showing empty channels within the PA layer. (B) A respective image with higlighted "channnels" - , possibly representing collapsed voids. The dotted lines in (A) and (B) represent the PA/PSf interface.

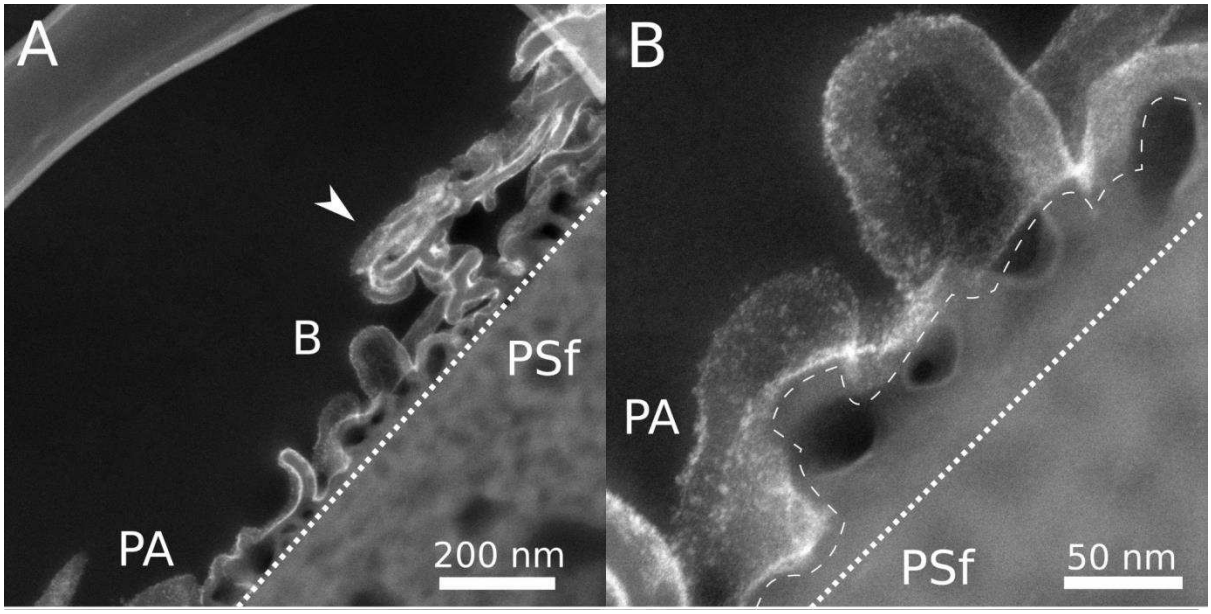

Figure 7 HAADF-STEM images of a wetted SW30HR membrane, which was vapour stained on the front side with RuO_4 for 1 min. (A) Stain precipitates formed on the surface and within convoluted regions (white arrowhead) of the PA layer. (B) Higher magnification image of the region seen in (A) showing stain within

the nano-film and a stain propagation front (dashed line). The dotted lines in (A) and (B) represent the PA/PSf interface.

3.3. Porosity of the polyamide nano-film

Until now the presence and dimensions of sub-nanometre pores within the PA nano-film have been estimated *via* indirect techniques, such as PALS [5]. The observation of <1 nm pores has been significantly hindered by intrinsic low contrast of polymer material and shortcomings of imaging techniques. With the combination of high spatially resolved EM imaging and staining methods described above, <1 nm pores can be visualised. The stain highlights circular regions within the PA nano-film (Figure 8). This contrast arises from stain precipitates lodged within the nano-film.

For high resolution STEM imaging, regions where precipitates had formed within the PA nano-film (stained with method II and III) were selected. Only sections with the stain evenly distributed across the cross-section were examined to ensure that the observed precipitates were inside the PA nano-film and not on its surface. The micrographs show the presence of precipitates within the PA nano-film (Figure 8). Both images show a fragment of a PA nodule at high magnification (SI Figure 8). The average diameter of precipitates formed within the nano-film is <1 nm (0.7±0.4 nm for vapour stained; 0.6±0.4 nm for liquid stained; n=250).

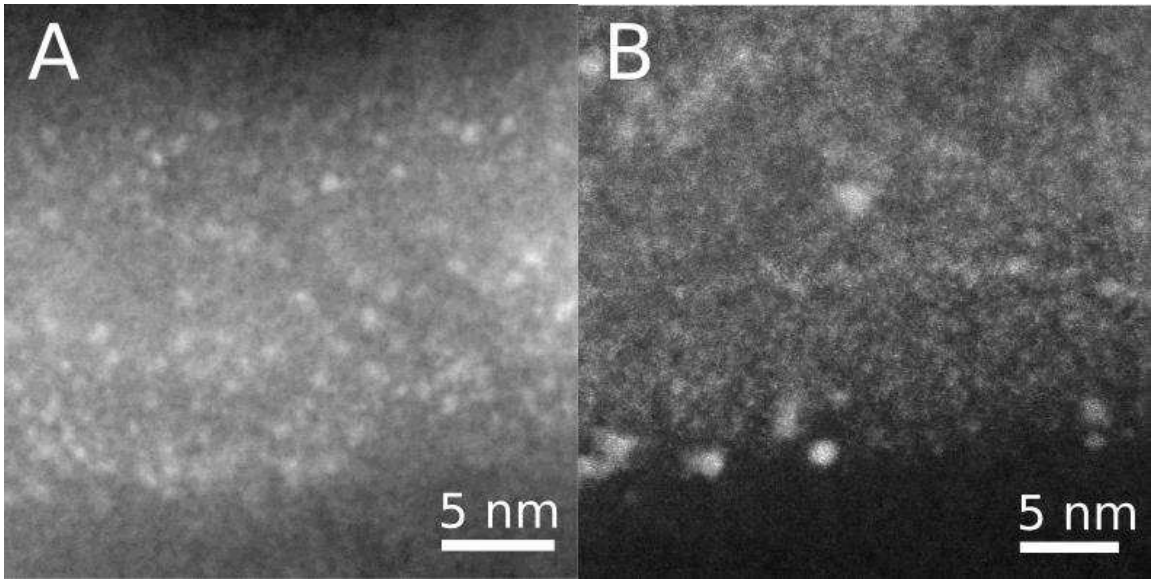

Figure 8 HAADF-STEM images of stain precipitates in the PA nano-films of the SW30HR membrane exposed to (A) the vapour and (B) liquid stain for 1 min (method II and III). Both images show cross-sections through the protuberances at high magnification (SI Figure 8).

4. Discussion

Staining combined with high resolution EM has provided several important advances in our understanding of the structure-related mechanisms by which the filtration occurs. Since direct, nano-scale observations of RO membranes in operating conditions are so far virtually impossible, we attempted to capture the changes in membrane behaviour using a tracer stain. The permeation through the PA layer depends on many factors, such as the accessible surface area of the PA layer and the nature of transport pathways within the PA layer and the 10 nm PA nano-film.

Using high resolution FIB-SEM 3-D reconstructions, we showed that the highly complex structures of the PA layer have a much larger active surface area than when examined *via* AFM. The behaviour of tracers within the dry and wet PA highlights the role of water solvation and swelling in activating the transport pathways. Finally, at the sub-nano-scale, we visualised <1 nm pore-like structures within

the PA nano-film using heavy metal staining. These observations lead to important conclusions about the membrane behaviour during the permeation and the role of water during this process.

4.1. 3-D reconstructions of the polyamide layer

FIB-SEM was used to obtain 3-D reconstructions of membrane morphology with resolution comparable with the resolution of low magnification TEM imaging [14]. Discrete voids within the PA layer observed with FIB-SEM correspond in size (average 20 nm) to those observed in a previous electron microscopy studies [19,20]. We build on the aforementioned studies by focusing on reconstruction of the surrounding PA envelope and studying the distribution and interconnectivity of voids within the PA envelope. Additionally, the heavy metal staining methods used allowed for more robust and automated thresholding, which enabled a straightforward quantification of the structural parameters of the PA layer and void spaces.

Large empty spaces under the ridges of the PA layer, which might be easily accessible to fluids (Figure 1D), as well as smaller, discrete voids within the PA envelope (Figure 2) were observed. While cross-sectional studies tend to assume all voids observed in the image are discrete [20], it is important to highlight that some of the voids within the PA layer, which appear discrete in the 2-D cross-sectional images, are open to either of the surfaces (but not both – Figure 1D, SI Movie 1, Figure SI 4). The presence of large empty spaces under the ridges increases the active surface of the membrane, which in turn may affect the water flux. The range of morphologies of the protuberances and their impact on separation performance have been reported on in previous studies [9,37–40], but until now have not been accurately quantified. We calculated structural parameters of the PA layer such

as local thickness or relative area ratio and compared the results with AFM data.

It has been shown that while AFM is commonly used in the characterisation of RO membranes [37,41], it significantly underappreciates the complexity of the PA layer. Using a SW30HR membrane, we showed that the actual front surface area might be 2.5-4 times larger than when estimated with dry AFM. Similarly, the SA/V ratio might be 2-3 times greater. On the other hand, the morphology of the rear side agreed with previous studies [42] and the surface area of the rear sides of the PA layer was comparable between FIB-SEM and AFM measurements.

Structures observed with SEM could be linked with lower hierarchy structures observed with TEM to enable a multi-scale mapping and to establish a hierarchical model of RO membranes. Cross-sections of FIB-SEM reconstructions can be correlated to TEM micrographs (compare Figure 1C with Figure 4A and Figure 5A). It is important to note that FIB-SEM has limited capability to resolve the internal structures in the PA layer (*i.e.,* stacked membrane folds or smaller voids), due to small contrast variations between the internal regions. Therefore, we propose FIB-SEM should be utilised as a tool to estimate the structural properties of the PA layer envelope (the volume within the external surface of the PA layer).

4.2. Nano-scale effects of staining

RuO_4 stains polymers that contain aromatic rings, amine/amide groups or unsaturated carbohydrates [43]. While the bulk effects of RuO_4 staining are well known and described [43], experiments using RuO_4 to study permeation pathways into RO membranes, have not previously been conducted. By analogy to polyethylene [44,45], we suggest that RuO_4 would oxidise the carbonyl and amide groups of polyamide. While this process alters the chemical composition of the stained film, it fixes and stabilises the structure by forming additional

crosslinks between oxidised functional groups. RuO_4 will move through the polymer network until it oxidises one of the chemical groups, limiting the pathway for diffusion of other molecules. At this stage, precipitates (larger clusters of ruthenium oxides) will form within the PA film. Therefore, the stain propagation is expected to be a function of diffusion and reactivity within the PA film. Upon membrane hydration, the staining of the film became more extensive (Figure 4D, Figure 7B, Figure 5B). In the aqueous environment, the PA film swells and enables further stain propagation within the membrane, facilitated by RuO_4-water interactions.

Nanocrystals of RuO_2 were also found to precipitate on external surfaces of the polymer [46]. This phenomenon occurs for all staining conditions (wet and dry) and is expected upon reduction of unstabilised RuO_4. This process occurs alongside the film staining and increases with exposure time (SI Figure 7). A short exposure of 1 min was selected to provide suitable contrast to image the nanostructure of the PA film.

At higher magnification, TEM images of the PA layer cross-sections revealed the presence of "channels" within the PA structure. These structures were identified as hollow regions, possibly formed by tight folding of the PA film. The presence of "channels" was further confirmed by wet staining experiments. Staining patterns (Figure 5) suggest that many of the finger-like structures observed in the TEM images should be considered as "deflated balloons" rather than solid nodules. Staining of each individual "channel" may vary depending on its openness. Empty "channels" would be visible if the surrounding membranes hindered all diffusing RuO_4. Filled "channels" would form if some of the RuO_4 passed through the PA film without oxidation of any functional group in the PA network and precipitated in the "channel" space. Importantly, "channels" were observed not only in the protuberances on the front side of the PA layer, but also in

the loops of the basal regions (Figure 5D). Regions, in which "channels" are visible, might have been formed from a highly crumpled single nano-film as suggested by Karan *et al.* [15]. In Figure 9, a schematic of features observed in the PA layer is shown.

A number of studies shows cave-like protuberances, which agrees with the crumpled nano-film model [6,16,19]. However, not all of the structures observed in the PA layer could be simply explained by film crumpling. Some of the studies report the presence of discrete voids [19,20]; in particular, Pacheco *et al.* [19] visualised these voids from reconstructed electron tomograms and attributed formation of discrete voids to the presence of aqueous droplets during interfacial polymerisation processes. Studies, in which this explanation of void formation was proposed previously [47,48], describe voids of micrometre (or greater) in size - orders of magnitude higher than our case.

The smallest voids reconstructed in our study were around 15 nm in diameter. Pacheco *et al.* also omitted reconstructing smaller voids due to difficulties with interpreting the contrast in the images and the resolution limit of electron tomography [49,50]. Smaller voids were definitely present, but it is not clear whether they were discrete or interconnected. We have made the same observation of both discrete and interconnected voids in our study. Future work using direct electron detectors and phase plates in electron microscopes will enable sufficient image resolution to establish whether some of these voids are in fact interconnected and to generate more complete model of the PA membrane.

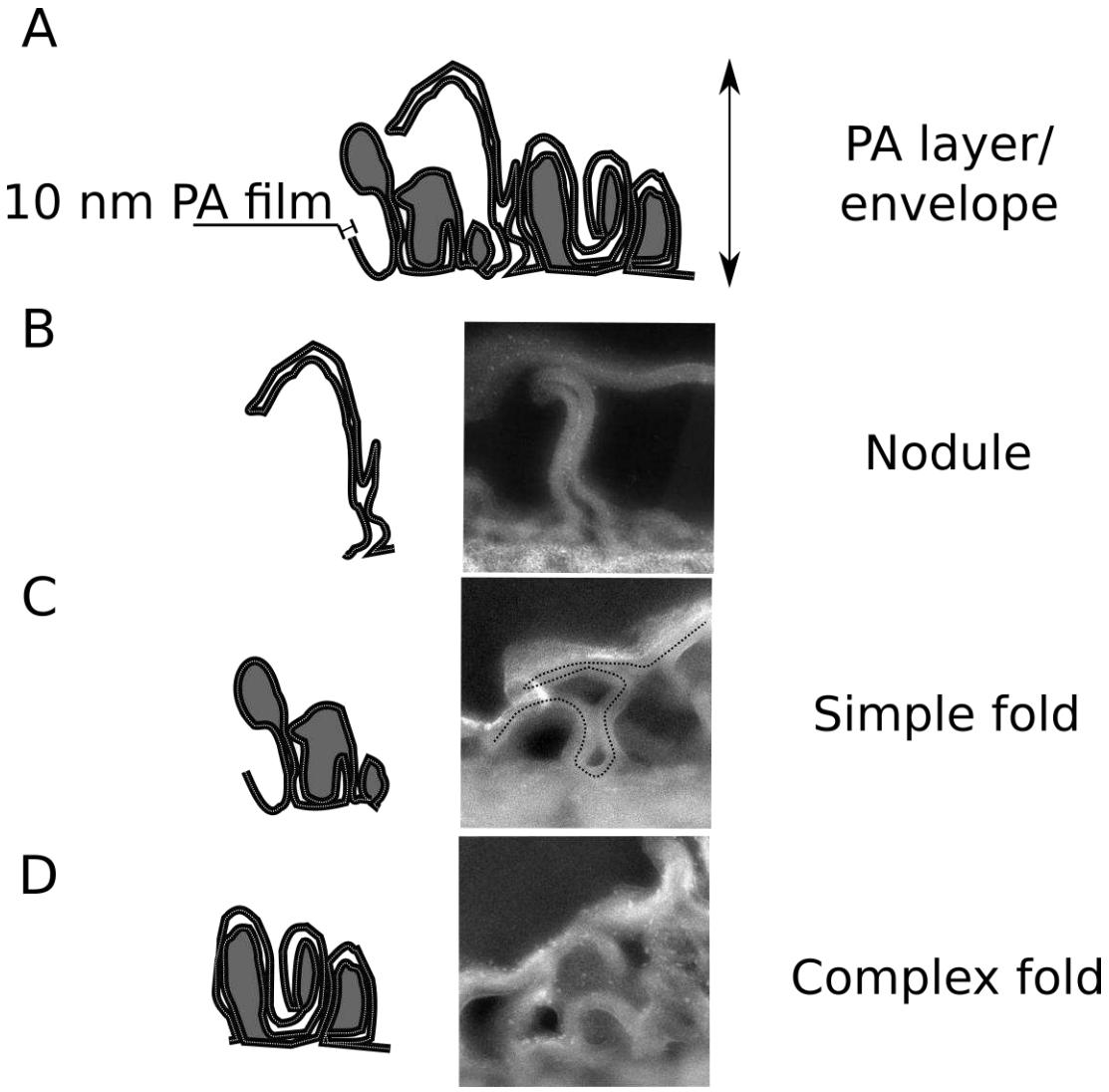

Figure 9 A schematic of features observed in 2-D cross-sections of the PA layer. (A) A general schematic of the ridge-valley structure. Individual features: (B) a nodule, (C) simple fold and (D) a complex fold. STEM images show fragments of the PA layer from top to PSf interface (white dashed line). The black, solid line represents the 10 nm crumpled, but continuous (dotted line) nano-film. Regions in grey can be interpreted as discrete holes. White regions within the PA layer are interpreted as "channels".

4.3. Sub-nanometer porosity

It has been suggested that nano-filtration through the membrane occurs within the PA nano-film itself as a result of sub-nanometre pores in the nano-film [4]. We attempted to visualise <1 nm diameter permeation pores within the PA nano-film by imaging the precipitates

using high resolution HAADF-STEM. The diameter of observed stain precipitates within the PA nano-film matches the pore sizes estimated with PALS [22,25,28] and calculated from molecular dynamics [26].

4.4. Connections between structure and performance

With the new data presented here we formulate a more accurate hypothesis about the behaviour of the PA structures in the aqueous environment. It was previously suggested that an increase in swelling correlates with increased permeability in membranes [37]. The reported swelling of the RO membranes (given as the difference between the thickness of wet and dry membranes observed in AFM) is usually in the range of 10-20 nm, possibly due to the rigidity of the cross-linked, aromatic PA [20,37,41]. If we take into account the morphology revealed by FIB-SEM, a few different mechanisms should be considered. These mechanisms may involve external- (stretching) and/or internally-driven (ballooning) expansion of the PA structures. Tentative mechanisms of swelling are sketched in Figure 10.

In the present study, we were able to visualise the penetration of water in the PA by using a stain tracer and elucidated the impact of water on tracer transport within the PA. We concluded that not all of the PA surfaces are immediately accessible and confirmed that water plays an important role in activating the free volume of the PA layer and nano-film. In the case of stain permeation, two effects can be observed: the opening of <1 nm pores within the PA nano-film and the opening of the larger voids, which may be considered discrete in the dry state, within the PA layer. Both phenomena might, in turn, facilitate ion permeation through the PA layer.

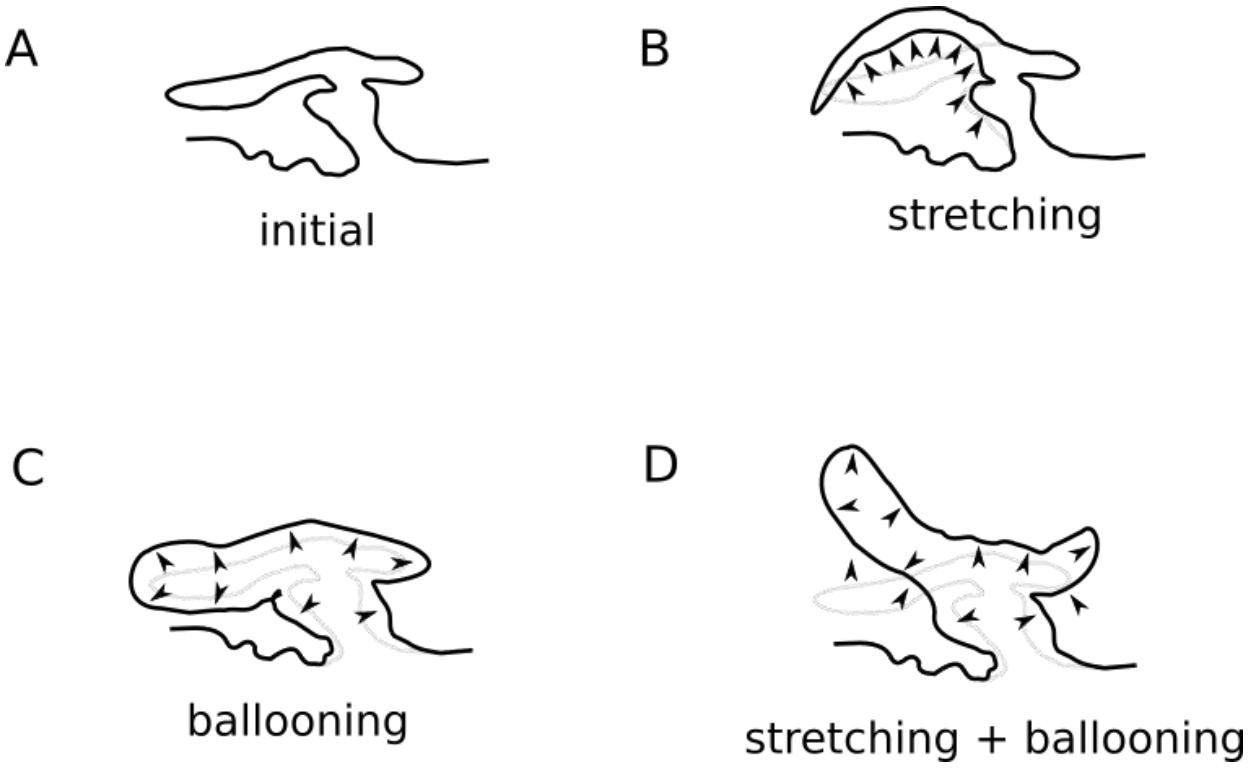

Figure 10 Possible responses of the PA structures to the presence of water. (A) The initial dry state. (B) Stretching – water acts externally, elongating some structures, but preserving the original shape the PA layer. (C) Ballooning – water acts internal filling and expanding the free volume of the PA layer. (D) Combined – water acts externally and internally.

5. Conclusions

In summary, the structural features of PA layer morphology in a representative RO membrane at the micro- and nano-scale have been visualised in 2-D and 3-D. The structural parameters of leaf-like sheets at the micro-scale were quantified. Their relation to the performance of membrane is discussed. Well-defined "channels" within the nodules, which have not previously been reported on, were imaged at the nano-scale. At the sub-nanometre scale, <1 nm pores were imaged. We believe our nano-scale results support the hypothesis that there is a nano-porous network underlying the filtration mechanics of the polyamide layer, which may be visualised using heavy metal staining. The staining in dry and wet conditions

also indicates the mechanism, by which water facilitates stain permeation through the PA layer. Tomographic studies of stained membranes provide new insight into the relationship between the structure and the membrane performance and open new possibilities for studying water flow and fouling in the vicinity of the PA layer *in silico*.

Acknowledgments

This research was funded by the BP International Centre for Advanced Materials (BP-ICAM). High resolution STEM imaging was conducted at the SuperSTEM Laboratory, the U.K National Facility for Aberration-Corrected STEM, supported by the Engineering and Physical Sciences Research Council (EPSRC). We thank Prof. Enrique Gomez for his helpful discussions.

References

[1] K.P. Lee, T.C. Arnot, D. Mattia, A review of reverse osmosis membrane materials for desalination—Development to date and future potential, J. Membr. Sci. 370 (2011) 1–22. doi:10.1016/j.memsci.2010.12.036.

[2] M. Elimelech, W.A. Phillip, The Future of Seawater Desalination: Energy, Technology, and the Environment, Science. 333 (2011) 712–717. doi:10.1126/science.1200488.

[3] R.J. Petersen, Composite reverse osmosis and nanofiltration membranes, J. Membr. Sci. 83 (1993) 81–150.

[4] T. Uemura, K. Kotera, M. Henmi, H. Tomioka, Membrane technology in seawater desalination: History, recent developments and future prospects, Desalination Water Treat. 33 (2011) 283–288. doi:10.5004/dwt.2011.2646.

[5] D.G. Cahill, V. Freger, S.-Y. Kwak, Microscopy and microanalysis of reverse-osmosis and nanofiltration membranes, MRS Bull. 33 (2008) 27–32.

[6] M. Kurihara, M. Hanakawa, Mega-ton Water System: Japanese national research and development project on seawater desalination and wastewater reclamation, Desalination. 308 (2013) 131–137. doi:10.1016/j.desal.2012.07.038.

[7] C.Y. Tang, Y.-N. Kwon, J.O. Leckie, Probing the nano-and micro-scales of reverse osmosis membranes—a comprehensive characterization of physiochemical properties of uncoated and coated membranes by XPS, TEM, ATR-FTIR, and streaming potential measurements, J. Membr. Sci. 287 (2007) 146–156.

[8] Y.-N. Wang, J. Wei, Q. She, F. Pacheco, C.Y. Tang, Microscopic Characterization of FO/PRO Membranes – A Comparative Study of CLSM, TEM and SEM, Environ. Sci. Technol. (2012) 120827103647009. doi:10.1021/es301885m.

[9] S.-Y. Kwak, S.G. Jung, Y.S. Yoon, D.W. Ihm, Details of surface features in aromatic polyamide reverse osmosis membranes characterized by scanning electron and atomic force microscopy, J. Polym. Sci. Part B Polym. Phys. 37 (1999) 1429–1440.

[10] B. Mi, O. Coronell, B. Marinas, F. Watanabe, D. Cahill, I. Petrov, Physico-chemical characterization of NF/RO membrane active layers by Rutherford backscattering spectrometry ☆, J. Membr. Sci. 282 (2006) 71–81. doi:10.1016/j.memsci.2006.05.015.
[11] Q. Li, X. Pan, C. Hou, Y. Jin, H. Dai, H. Wang, X. Zhao, X. Liu, Exploring the dependence of bulk properties on surface chemistries and microstructures of commercially composite RO membranes by novel characterization approaches, Desalination. 292 (2012) 9–18. doi:10.1016/j.desal.2012.02.005.
[12] V. Freger, A. Bottino, G. Capannelli, M. Perry, V. Gitis, S. Belfer, Characterization of novel acid-stable NF membranes before and after exposure to acid using ATR-FTIR, TEM and AFM, J. Membr. Sci. 256 (2005) 134–142.
[13] G.R. Guillen, Y. Pan, M. Li, E.M.V. Hoek, Preparation and Characterization of Membranes Formed by Nonsolvent Induced Phase Separation: A Review, Ind. Eng. Chem. Res. 50 (2011) 3798–3817. doi:10.1021/ie101928r.
[14] F.A. Pacheco, I. Pinnau, M. Reinhard, J.O. Leckie, Characterization of isolated polyamide thin films of RO and NF membranes using novel TEM techniques, J. Membr. Sci. 358 (2010) 51–59.
[15] S. Karan, Z. Jiang, A.G. Livingston, Sub–10 nm polyamide nanofilms with ultrafast solvent transport for molecular separation, Science. 348 (2015) 1347–1351. doi:10.1126/science.aaa1313.
[16] H. Yan, X. Miao, J. Xu, G. Pan, Y. Zhang, Y. Shi, M. Guo, Y. Liu, The porous structure of the fully-aromatic polyamide film in reverse osmosis membranes, J. Membr. Sci. 475 (2015) 504–510. doi:10.1016/j.memsci.2014.10.052.
[17] C. Kong, A. koushima, T. Kamada, T. Shintani, M. Kanezashi, T. Yoshioka, T. Tsuru, Enhanced performance of inorganic-polyamide nanocomposite membranes prepared by metal-alkoxide-assisted interfacial polymerization, J. Membr. Sci. 366 (2011) 382–388. doi:10.1016/j.memsci.2010.10.026.
[18] T. Kamada, T. Ohara, T. Shintani, T. Tsuru, Optimizing the preparation of multi-layered polyamide membrane via the addition of a co-solvent, J. Membr. Sci. 453 (2014) 489–497. doi:10.1016/j.memsci.2013.11.028.
[19] F. Pacheco, R. Sougrat, M. Reinhard, J.O. Leckie, I. Pinnau, 3D visualization of the internal nanostructure of polyamide thin films in RO membranes, J. Membr. Sci. (2015). doi:10.1016/j.memsci.2015.10.061.
[20] L. Lin, R. Lopez, G.Z. Ramon, O. Coronell, Investigating the void structure of the polyamide active layers of thin-film composite membranes, J. Membr. Sci. 497 (2016) 365–376. doi:10.1016/j.memsci.2015.09.020.
[21] J.G. Wijmans, R.W. Baker, The solution-diffusion model: a review, J. Membr. Sci. 107 (1995) 1–21.
[22] T. Fujioka, N. Oshima, R. Suzuki, W.E. Price, L.D. Nghiem, Probing the internal structure of reverse osmosis membranes by positron annihilation spectroscopy: Gaining more insight into the transport of water and small solutes, J. Membr. Sci. 486 (2015) 106–118. doi:10.1016/j.memsci.2015.02.007.
[23] S. Li, Z. Wang, C. Zhang, M. Wang, F. Yuan, J. Wang, S. Wang, Interfacially polymerized thin film composite membranes containing ethylene oxide groups for CO2 separation, J. Membr. Sci. 436 (2013) 121–131. doi:10.1016/j.memsci.2013.02.038.
[24] J. Albo, J. Wang, T. Tsuru, Gas transport properties of interfacially polymerized polyamide composite membranes under different pre-treatments and temperatures, J. Membr. Sci. 449 (2014) 109–118. doi:10.1016/j.memsci.2013.08.026.
[25] A. Shimazu, H. Goto, T. Shintani, M. Hirose, R. Suzuki, Y. Kobayashi, Vacancy profile in reverse osmosis membranes studied by positron annihilation lifetime measurements and molecular dynamics simulations, J. Phys. Conf. Ser. 443 (2013) 012050. doi:10.1088/1742-6596/443/1/012050.

[26] V. Kolev, V. Freger, Hydration, porosity and water dynamics in the polyamide layer of reverse osmosis membranes: A molecular dynamics study, Polymer. 55 (2014) 1420–1426. doi:10.1016/j.polymer.2013.12.045.
[27] M. Doi, S.F. Edwards, The Theory of Polymer Dynamics, Oxford : Clarendon, 1986.
[28] M. Henmi, Y. Fusaoka, H. Tomioka, M. Kurihara, High performance RO membranes for desalination and wastewater reclamation and their operation results, Water Sci. Technol. 62 (2010) 2134. doi:10.2166/wst.2010.396.
[29] K. Košutić, L. Kaštelan-Kunst, B. Kunst, Porosity of some commercial reverse osmosis and nanofiltration polyamide thin-film composite membranes, J. Membr. Sci. 168 (2000) 101–108.
[30] J. Stawikowska, A.G. Livingston, Nanoprobe imaging molecular scale pores in polymeric membranes, J. Membr. Sci. 413-414 (2012) 1–16. doi:10.1016/j.memsci.2012.02.033.
[31] R.W. Baker, Reverse Osmosis, in: Membr. Technol. Appl., 2nd ed, J. Wiley, Chichester ; New York, 2004: pp. 191–235.
[32] M. Doube, BoneJ, (n.d.). http://bonej.org/thickness.
[33] W.S. Rasband, ImageJ, (1997). http://imagej.nih.gov/ij/.
[34] M. Doube, M.M. Klosowski, I. Arganda-Carreras, F.P. Cordelières, R.P. Dougherty, J.S. Jackson, B. Schmid, J.R. Hutchinson, S.J. Shefelbine, BoneJ: Free and extensible bone image analysis in ImageJ, Bone. 47 (2010) 1076–1079. doi:doi:10.1016/j.bone.2010.08.023.
[35] T. Hildebrand, P. Ruegsegger, A new method for the model-independent assessment of thickness in three-dimensional images, J. Microsc. 185 (1997) 67–75.
[36] C.M. McGilvery, A.E. Goode, M.S.P. Shaffer, D.W. McComb, Contamination of holey/lacey carbon films in STEM, Micron. 43 (2012) 450–455. doi:10.1016/j.micron.2011.10.026.
[37] V. Freger, Swelling and Morphology of the Skin Layer of Polyamide Composite Membranes: An Atomic Force Microscopy Study, Environ. Sci. Technol. 38 (2004) 3168–3175. doi:10.1021/es034815u.
[38] A.K. Ghosh, B.-H. Jeong, X. Huang, E.M.V. Hoek, Impacts of reaction and curing conditions on polyamide composite reverse osmosis membrane properties, J. Membr. Sci. 311 (2008) 34–45. doi:10.1016/j.memsci.2007.11.038.
[39] M.L. Lind, A.K. Ghosh, A. Jawor, X. Huang, W. Hou, Y. Yang, E.M.V. Hoek, Influence of Zeolite Crystal Size on Zeolite-Polyamide Thin Film Nanocomposite Membranes, Langmuir. 25 (2009) 10139–10145. doi:10.1021/la900938x.
[40] J. Yin, E.-S. Kim, J. Yang, B. Deng, Fabrication of a novel thin-film nanocomposite (TFN) membrane containing MCM-41 silica nanoparticles (NPs) for water purification, J. Membr. Sci. 423-424 (2012) 238–246. doi:10.1016/j.memsci.2012.08.020.
[41] E. Dražević, K. Košutić, V. Freger, Permeability and selectivity of reverse osmosis membranes: Correlation to swelling revisited, Water Res. 49 (2014) 444–452. doi:10.1016/j.watres.2013.10.029.
[42] J. Lee, A. Hill, S. Kentish, Formation of a thick aromatic polyamide membrane by interfacial polymerisation, Sep. Purif. Technol. 104 (2013) 276–283. doi:10.1016/j.seppur.2012.11.015.
[43] J.S. Trent, J.I. Scheinbeim, P.R. Couchman, Ruthenium tetraoxide staining of polymers for electron microscopy, Macromolecules. 16 (1983) 589–598.
[44] H. Sano, T. Usami, H. Nakagawa, Lamellar morphologies of melt-crystallized polyethylene, isotactic polypropylene and ethylene-propylene copolymers by the RuO4 staining technique, Polymer. 27 (1986) 1497–1504.
[45] H.. Haubruge, A.. Jonas, R. Legras, Staining of poly(ethylene terephthalate) by ruthenium tetroxide, Polymer. 44 (2003) 3229–3234. doi:10.1016/S0032-3861(03)00255-6.
[46] T.M. Chou, P. Prayoonthong, A. Aitouchen, M. Libera, Nanoscale artifacts in RuO 4-stained poly (styrene), Polymer. 43 (2002) 2085–2088.
[47] L.J.J.M. Janssen, K. te Nijenhuls, Encapsulation by interfacial polycondensation. I. The capsule production and a model for wall growth, J. Membr. Sci. 65 (1992) 59–68.

[48] F. Yuan, Z. Wang, X. Yu, Z. Wei, S. Li, J. Wang, S. Wang, Visualization of the Formation of Interfacially Polymerized Film by an Optical Contact Angle Measuring Device, J. Phys. Chem. C. 116 (2012) 11496–11506. doi:10.1021/jp210209v.
[49] P.A. Midgley, R.E. Dunin-Borkowski, Electron tomography and holography in materials science, Nat. Mater. 8 (2009) 271–280. doi:10.1038/nmat2406.
[50] C.A. Diebolder, A.J. Koster, R.I. Koning, Pushing the resolution limits in cryo electron tomography of biological structures: PUSHING THE RESOLUTION LIMITS IN CRYO ELECTRON TOMOGRAPHY, J. Microsc. 248 (2012) 1–5. doi:10.1111/j.1365-2818.2012.03627.x.